arXiv:0910.3106v3 [cond-mat.mes-hall] 8 Feb 2010

Tunable electronic transport and unidirectional quantum wires in graphene subjected to electric and magnetic fields

Yury P. Bliokh,[1,2] Valentin Freilikher,[1,3] and Franco Nori[1,4]

[1] *Advanced Science Institute, The Institute of Physical and Chemical Research (RIKEN), Wako-shi, Saitama 351-0198, Japan*
[2] *Department of Physics , Technion-Israel Institute of Technology, Haifa 32000, Israel*
[3] *Jack and Pearl Resnick Institute of Advanced Technology, Department of Physics, Bar-Ilan University, Ramat-Gan 52900, Israel*
[4] *Department of Physics, University of Michigan, Ann Arbor, Michigan 48109-1040, USA.*

Magnetic barriers in graphene are not easily tunable. Here we show that the application of both electric and magnetic fields provides tunable and far more controllable electronic states in graphene. In particular, a one-dimensional channel (quantum wire) can be created, which supports localized electron-hole states with parameters tunable by the electric field. Such quantum wire offers peculiar conducting properties, like unidirectional conductivity and robustness to disorder. Two separate quantum wires comprise a waveguide with two types of eigenmodes: one type is similar to traditional waveguides, the other type is formed by coupled surface waves propagating along the boundaries of the waveguide.

PACS numbers: 71.10.Fd, 73.20.Fz, 73.23.-b

I. INTRODUCTION

The realization of stable single-layer carbon crystals (graphene) triggered an explosion of interest in this material because of its unique electronic properties (for reviews see, e.g., [1–3]), making it a promising candidate for designing one-chip nanoelectronic devices (e.g., [2, 4–7]). However, Klein tunneling [8] hinders the application of traditional methods of current control (e.g., on-off switching, changing the current direction, etc.) by tuning the voltage between various elements of a device [9]. This effect also complicates the creation of localized electron-hole states in graphene.

As it was shown recently [10, 11], this difficulty in creating localized states can be overcome by using an inhomogeneous magnetic field. An alternative way (which is mathematically analogous to the previous one), involving graphene sheet deformations, was proposed in [12–14]. The regions with either inhomogeneous magnetic field or strains can act as non-transparent barriers and angle-resolved charge carriers filters [15] and form long-lived [16] or stationary localized states [10, 11, 17, 18]. These 1-D states appear as "surface" waves propagating along the inhomogeneity of the magnetic field [19–24], or along the strains [12].

The charge-confining and guiding capabilities of magnetic barriers [10, 11] and graphene strains [12] open up certain possibilities for potential future applications. However when it comes to designing fast-tunable electronic devices (switches, filters, etc.) a difficulty emerges. The problem is that most of the existing magnetic barrier technologies usually imply the deposition (on top or beneath the graphene sheet) of a *fixed* pattern of magnetic material which reproduces the desired magnetic field distribution in the sample. Any change of parameters means in fact building a new setup and creates formidable (if surmountable) obstacles for harnessing magnetic barriers as elements of fast-acting electronic devices. In other words, magnetic barriers are not easily tunable.

Here we suggest an efficient way around this problem by simultaneously employing both inhomogeneous magnetic and electric fields: i.e., *combined electric and magnetic barriers*. The proper combination of these two allows a better control of the transport properties of graphene by tuning the electric potential, with the parameters of the magnetic field remaining intact. Depending on the voltage, this barrier can be either semitransparent or opaque.

The combined electrostatic and magnetic barrier possesses a unique feature that makes it different from other types of barriers. Graphene with mutually perpendicular electric and magnetic fields supports states which are localized near the barrier. These current-carrying states (surface waves) correspond to quasiparticles moving along the barrier just in one direction. The direction and the value of the quasiparticle velocity is easily controlled by the electrostatic potential. These states correspond to the classical drift of charged particles in crossed electric and magnetic fields and exist if and only if the drift velocity is smaller than the Fermi velocity. The absence of counter-propagating states prevents the backscattering induced by either irregularities in graphene [25–27] or by the fluctuations of the magnetic field. For more about the effects of disorder on the electronic properties of graphene see Chapter IV in [1] and references therein.

While one barrier forms a wire, two such barriers make up a waveguide. This waveguide has a set of "ordinary" waves and another set of "extraordinary" waves. The ordinary waves are characterized by the quantization of their transverse wave numbers, while the extraordinary waves are formed by two coupled surface waves propagating along the waveguide walls (barriers). Depending on the barrier parameters, the extraordinary modes can be either bidirectional or unidirectional. There is an energy

gap where only extraordinary modes exist. Decreasing the spacing between the barriers broadens this gap. The extraordinary modes are also stable against backscattering.

The unique, easily controllable, and tunable features of the combined barriers and waveguides are promising toward creating new graphene-based electronic devices.

This paper is organized as follows. In Sec. II, the models for the electromagnetic barriers and auxiliary constructions are described. In Sec. III, the properties of a single electromagnetic barrier are studied. The spectrum and eigenfunction of the waveguide formed by two barriers are presented in Sec. IV. Concluding remarks are in Sec. V.

II. BASIC FORMALISM

A. Step-like barrier.

The low-energy excitations in single-layer graphene in the presence of a perpendicular to the layer magnetic field $H_z(x) = dA_y/dx$ and an in-plane electric field $E_x(x) = -dV(x)/dx$ (which are constant along the y-direction) are described by the Dirac equations:

$$\left[-i\frac{\partial}{\partial x} + \frac{\partial}{\partial y} + \frac{ie}{c\hbar}A(x)\right]\psi_A = \frac{1}{v_F\hbar}[\mathcal{E} - eV(x)]\psi_B,$$
$$\left[-i\frac{\partial}{\partial x} - \frac{\partial}{\partial y} - \frac{ie}{c\hbar}A(x)\right]\psi_B = \frac{1}{v_F\hbar}[\mathcal{E} - eV(x)]\psi_A \quad (1)$$

where $A(x)$ is the y-component of the vector potential, $V(x)$ is the scalar potential, $\mathcal{E}$ is the energy of the quasiparticle, and ψ is the two-component spinor $\psi = (\psi_A, \psi_B)^T$.

Let us consider two homogeneous graphene domains subjected to different constant scalar (V_1 and V_2) and vector ($A_{y1} \equiv A_1$ and $A_{y2} \equiv A_2$) potentials, and assume that the domains are connected by an inhomogeneous transition region where the potentials vary smoothly between the constant values (see Fig. 1). When the width ℓ of this region is large compared to the graphene lattice spacing a, and small compared to the Fermi wavelength λ_F ($a \ll \ell \ll \lambda_F$), the potentials can be replaced by step-like functions, as shown by the red dashed line in Fig. 1. This widely used approximation simplifies the problem considerably.

Due to translational invariance along the y-direction, the solutions of Eqs. (1) can be presented in the form $\psi_{A,B}(x,y) = \exp(ik_y y)\Psi_{A,B}(x)$. In dimensionless variables $\xi = x/L$,

$$\kappa_\perp = k_y L, \quad \varepsilon = \mathcal{E}L/\hbar v_F,$$

$$u = eVL/\hbar v_F, \quad \mathcal{A} = (eL/c\hbar)A,$$

where L is a characteristic spatial scale (magnetic length $\ell_H = \sqrt{c\hbar/eH}$, for instance), Eqs. (1) have the form:

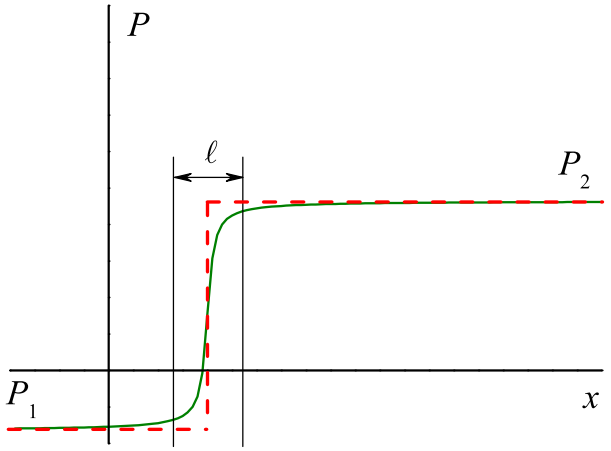

FIG. 1: (color online) Schematic diagram of the inhomogeneity region between two otherwise-homogeneous graphene sheets. The function $P(x)$ can be either the electric scalar $V(x)$ or magnetic $A(x)$ potential (hence the choice of P). Here, $P(x \to -\infty) \to P_1$, and $P(x \to \infty) \to P_2$. The dashed line is the step-like barrier approximation. Note that $\boldsymbol{A} \equiv A_y\hat{\boldsymbol{y}} \equiv A(x)\hat{\boldsymbol{y}}$.

$$\left(\frac{d}{d\xi} - \kappa_\perp - \mathcal{A}\right)\psi_A = i(\varepsilon - u)\psi_B,$$
$$\left(\frac{d}{d\xi} + \kappa_\perp + \mathcal{A}\right)\psi_B = i(\varepsilon - u)\psi_A. \quad (2)$$

B. Homogeneous graphene.

In homogeneous graphene ($\mathcal{A}$ = constant, u = constant), $\Psi_{A,B}(\xi) \sim \exp(i\kappa_\parallel\xi)$, and the wave vector components $\kappa_\parallel$ and $\kappa_\perp$ are related by the dispersion relation:

$$\kappa_\parallel^2 + (\kappa_\perp + \mathcal{A})^2 = (\varepsilon - u)^2. \quad (3)$$

This equation is valid for both propagating ($\mathrm{Im}\kappa_\parallel = 0$) and non-propagating (evanescent) waves ($\mathrm{Re}\kappa_\parallel = 0$). In the $(\kappa_\parallel, \kappa_\perp)$-plane, the wave vectors $\boldsymbol{\kappa}$ of the propagating waves lie on a circle centered at the point $\kappa_\perp = -\mathcal{A}$, with radius $\rho = |\varepsilon - u|$ (Fig. 2). For given $\kappa_\perp$ and ε, there are two solutions of the dispersion equation (3) with positive (blue solid arrow in Fig. 2) and negative (blue dashed arrow in Fig. 2) values of $\kappa_\parallel$.

C. Probability current.

The solutions of Eq. (2) have the form:

$$\Psi_{A,B} = \psi_{A,B}^{(+)}e^{i\kappa_\parallel\xi} + \psi_{A,B}^{(-)}e^{-i\kappa_\parallel\xi}. \quad (4)$$

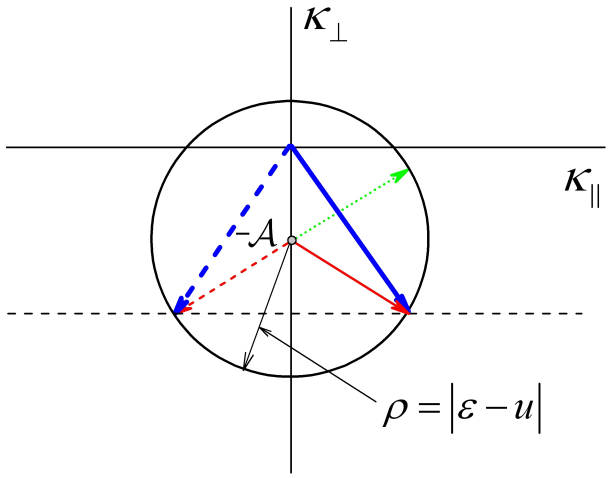

FIG. 2: (color online) The wave vectors $\boldsymbol{\kappa}$ (blue thick arrows) of propagating waves in homogeneous graphene lie on a circle, described by the dispersion equation (3). The normalized coefficients $\rho C^{(+)}$ (red solid arrow) and $\rho C^{(-)}$ (red dashed arrow) are shown when $\mathrm{sgn}(\varepsilon - u) = +1$. The current with positive J_x component is directed either along the solid red arrow when $\mathrm{sgn}(\varepsilon - u) = +1$, or along the green dotted arrow when $\mathrm{sgn}(\varepsilon - u) = -1$.

The amplitudes $\psi^{(\pm)}_{A,B}$ are connected by the relation:

$$\psi^{(\pm)}_B = C^{(\pm)}\psi^{(\pm)}_A, \tag{5}$$

where

$$C^{(\pm)} = \frac{i(\kappa_\perp + \mathcal{A}) \pm \kappa_\parallel}{\varepsilon - u}, \tag{6}$$

and

$$C^{(-)} = -1/C^{(+)}. \tag{7}$$

Eq. (5) allows the consideration of the spinor component Ψ_A only (thereafter Ψ). When the wave vector $\boldsymbol{\kappa}$ lies on the circle (propagating waves), the following representation of the coefficients $C^{(\pm)}$ is valid:

$$C^{(+)} \equiv C = \mathrm{sgn}(\varepsilon - u)e^{i\varphi}, \quad C^{(-)} = -C^*, \tag{8}$$

where

$$\sin\varphi = \frac{\kappa_\perp + \mathcal{A}}{|\varepsilon - u|}, \qquad \cos\varphi = \frac{\kappa_\parallel}{|\varepsilon - u|}. \tag{9}$$

The angle φ is connected with the direction of the probability current density, $\boldsymbol{J}$ [10, 11]. Indeed, the probability current density $\boldsymbol{J} = \langle\psi|\boldsymbol{\sigma}|\psi\rangle$ can be presented in the form:

$$J_x + iJ_y = 2\psi^*_A\psi_B. \tag{10}$$

Using Eq. (10), the current densities $\boldsymbol{J}^{(\pm)}$ that correspond to pure (+) and (−) states, can be written as:

$$\begin{aligned} \boldsymbol{J}^{(+)} &= 2\,\mathrm{sgn}(\varepsilon - u)e^{i\varphi}\left|\psi^{(+)}\right|^2, \\ \boldsymbol{J}^{(-)} &= -2\,\mathrm{sgn}(\varepsilon - u)e^{-i\varphi}\left|\psi^{(-)}\right|^2. \end{aligned} \tag{11}$$

It follows from Eq. (11) that the current with positive component $J_x > 0$ is described by $\psi^{(+)}$ when $\mathrm{sgn}(\varepsilon - u) = +1$ (red arrow in Fig. 1), and by $\psi^{(-)}$ when $\mathrm{sgn}(\varepsilon - u) = -1$ (green arrow in Fig. 1).

III. COMBINED ELECTRIC AND MAGNETIC BARRIER

A. Semi-transparent barrier.

The continuity condition for the spinor components $\Psi_{A,B}$ on the interface between two homogeneous domains (domain 1 and domain 2) can be written in the form:

$$(\psi^{(+)}_2, \psi^{(-)}_2)^T = \hat{M}(\psi^{(+)}_1, \psi^{(-)}_1)^T, \tag{12}$$

where $\hat{M}$ is the transfer matrix:

$$\hat{M} = \frac{1}{C_2 + C_2^{-1}} \begin{Vmatrix} C_2^{-1} + C_1 & C_2^{-1} - C_1^{-1} \\ C_2 - C_1 & C_2 + C_1^{-1} \end{Vmatrix}. \tag{13}$$

The coefficients $C_{1,2}$ are defined by Eqs. (6)–(8), with potentials $u_{1,2}$ and $\mathcal{A}_{1,2}$, correspondingly.

To describe the transport properties at the barrier, we now introduce a graphic representation, shown in Fig. 3, which provides a better understanding of the dispersion relations. In Fig. 3, points on the circles represent solutions of the dispersion equations in domains 1 and 2, and correspond to propagating waves (waves with real $\kappa_\parallel$) in these domains.

Let us now consider the "refraction law" which relates the directions of the incident and refracted waves [states with the same sign of the current component J_x in both domains (for definiteness, $J_x > 0$)]. This "refraction law" can be easily derived with the help of Fig. 3 as follows. Due to translation invariance along the y-axis, the wave vector component $\kappa_\perp$ has the same value in both media. The wave vectors $\boldsymbol{\kappa}$ of the propagating waves take on values $\boldsymbol{\kappa}_1$ and $\boldsymbol{\kappa}_2$ in the first and second domains. The wave vectors $\boldsymbol{\kappa}_1$ and $\boldsymbol{\kappa}_2$ lie at the intersection of the corresponding circles and the line $\kappa_\perp = \text{constant}$ (thin horizontal dashed black line in Fig. 3). There are two such intersections for each of the two circles. The physically meaningfull intersections (i.e., the intersections that present the solutions with positive current density component $J_x > 0$) are defined by the sign of $(\varepsilon - u_{1,2})$. The currents $\boldsymbol{J}$ are directed either along the radius vector (i.e., the vectors from the centers of both circles to the intersections, in Fig. 3) of the intersection or in the opposite direction, depending on the sign of: $(\varepsilon - u_{1,2})$. For example, when $\mathrm{sgn}(\varepsilon - u_1) = +1$, the incident current $\boldsymbol{J}$ is directed along the red arrow in Fig. 3. The refracted current is directed along the blue arrow when $\mathrm{sgn}(\varepsilon - u_2) = +1$, or along the green arrow when $\mathrm{sgn}(\varepsilon - u_2) = -1$.

The following relation defines the connection between the incident, θ_1, and refracted, θ_2, angles:

$$\kappa_\perp = -\mathcal{A}_1 - (\varepsilon - u_1)\sin\theta_1 = -\mathcal{A}_2 - (\varepsilon - u_2)\sin\theta_2. \tag{14}$$

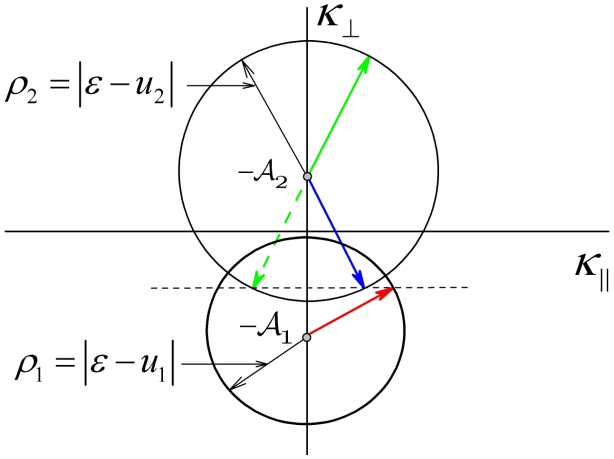

FIG. 3: (color online) Here $\kappa_\perp$ and $\kappa_\parallel$ are the transverse and longitudinal components of the wave vector $\boldsymbol{\kappa}$. The circles represent solutions of the dispersion relations $\varepsilon(\boldsymbol{\kappa})$ in the domains 1 and 2, and correspond to propagating waves. The top circle has a radius $\rho_2 = |\varepsilon - u_2|$, while the bottom circle has a radius $\rho_2 = |\varepsilon - u_2|$. The incident current is directed along the bottom-right red arrow. The refracted current is directed along the blue arrow (the only arrow pointing South-East, towards 5 o'clock), when $\mathrm{sgn}(\varepsilon - u_2) = +1$, and along the green solid arrow (pointing North-East, 1 o'clock) when $\mathrm{sgn}(\varepsilon - u_2) = -1$. The latter one is opposite to the dashed (South-West, 7 o'clock) green one, which intersects the black horizontal dashed line.

When, forinstance, $|\varepsilon - u_1| = |\varepsilon - u_2| \equiv |\varepsilon - u|$, the refraction law reads:

$$\mathrm{sgn}(\varepsilon - u_1)\sin\theta_1 + \mathrm{sgn}(\varepsilon - u_2)\sin\theta_2 = \frac{\mathcal{A}_2 - \mathcal{A}_1}{|\varepsilon - u|}. \quad (15)$$

The refraction law presented in [10, 11] is a particular case ($u_1 = u_2 = 0$) of this relation.

It is possible to show that the transmission coefficient $T = J_{x\,1}/J_{x\,2}$ is defined by the following expression:

$$T \equiv T\,(w_2, w_1) = \frac{2\sqrt{1-w_2^2}\sqrt{1-w_1^2}}{1 + \sqrt{1-w_2^2}\sqrt{1-w_1^2} - w_2 w_1}, \quad (16)$$

where

$$w_{2,1} = \frac{\kappa_\perp + \mathcal{A}_{2,1}}{\varepsilon - u_{2,1}}.$$

It follows from Eq. (16) that

$$T|_{w_2 = w_1} = 1, \quad (17)$$

i.e., there is an angle of incidence, non-normal in the general case, for which the interface is totally transparent. In other words, the barrier changes the direction of incidence, at which Klein tunneling occurs [28].

B. Non-transparent barrier: bound states.

When the difference between the vector potentials is large enough,

$$|\mathcal{A}_1 - \mathcal{A}_2| > |\varepsilon - u_1| + |\varepsilon - u_2|, \quad (18)$$

the circles in Fig. 3 do not cross, and no propagating wave can penetrate through the interface. Therefore, the transmission coefficient is equal to zero, $T = 0$, and the barrier is nontransparent (reflecting wall). However, it can support a wave, which propagates *along* the line separating two domains with the amplitude exponentially decaying in the transverse directions. This mode is a 1D analog of two-dimensional surface waves. In order to simplify terminology, in what follows, we call it a surface wave.

Let us now determine the properties and existence conditions of these surface waves. When the wave vector components $\kappa_{\parallel\,j}$ $(j = 1, 2)$ in both media are imaginary, $\kappa_{\parallel\,j} = i|\kappa_{\parallel\,j}|$ the wave functions $\psi_{1,2}$ have the form:

$$\psi_j = \psi_j^{(+)} e^{-|\kappa_{\parallel\,j}|\xi} + \psi_j^{(-)} e^{+|\kappa_{\parallel\,j}|\xi}, \quad (19)$$

where $\kappa_{\parallel\,j} = \sqrt{(\varepsilon - u_j)^2 - \kappa_\perp^2} = i\sqrt{\kappa_\perp^2 - (\varepsilon - u_j)^2}$. The wave is now localized near the interface $\xi = 0$ when $\psi_1^{(-)} = \psi_2^{(+)} = 0$, i.e. $\psi_2^{(+)} = M_{11}\psi_1^{(+)} = 0$. Therefore, the condition

$$M_{11} = \frac{C_1 C_2 + 1}{C_2^2 + 1} = 0 \quad (20)$$

is the dispersion relation of the surface waves. A solution $\varepsilon(\kappa_\perp)$ of this equation exists if and only if

$$\left|\frac{u_1 - u_2}{\mathcal{A}_1 - \mathcal{A}_2}\right| < 1 \quad (21)$$

and has the form:

$$\varepsilon(\kappa_\perp) = \frac{u_1\mathcal{A}_2 - u_2\mathcal{A}_1}{\mathcal{A}_2 - \mathcal{A}_1} + \kappa_\perp \frac{u_1 - u_2}{\mathcal{A}_2 - \mathcal{A}_1}. \quad (22)$$

Equation (22) describes a surface wave propagating along the line $\xi = 0$, with the group velocity $\nu_g \sim d\varepsilon/d\kappa_\perp = (u_1 - u_2)/(\mathcal{A}_2 - \mathcal{A}_1)$.

Note that the inequality (21) in the dimensional variables takes the form:

$$\frac{c}{v_F}\left|\frac{\Delta V}{\Delta A}\right| < 1, \quad (23)$$

where ΔV and ΔA are, respectively, the differences between the scalar and vector potentials in the two graphene domains. From Fig. 1 one can see that the electric field in the inhomogeneous region is $E_x \simeq -\Delta V/\ell$, and the magnetic field is $H_z \simeq \Delta A/\ell$. Therefore, the inequality (23) can be written as:

$$v_d \equiv c\left|\frac{E_x}{H_z}\right| < v_F. \quad (24)$$

Thus, the dimensional group velocity $v_g = \hbar^{-1} d\mathcal{E}/dk_y$ of the surface wave, coincides with the *drift velocity* $v_d = cE/H$ of a charged particle in crossed electric and magnetic fields.

If, for example, the characteristic width, ℓ, of the barrier (see Fig. 1) is $\ell = 10$nm, and the magnetic field $H_z = 1$ T, the condition for the surface wave to exist,$v_d < v_F$ [Eq. (24)], is satisfied when the potential difference across the barrier (between two graphene domains in Fig. 1) is $\Delta V = 10$mV or less. These numbers are quite feasible. Magnetic barriers with amplitudes of up 1 T have been created experimentally by depositing ferromagnetic films on top of a graphene sheet [29, 30]. Patterened stripes down to 10nm can be realized using nanolitography (see [31] for review).

Note that the bound state near the δ-function magnetic barrier [$H_z \sim \delta(x)$] described in [15] is the particular case $u_1 = u_2$ ($E_x = 0$) of this surface wave with zero group velocity.

C. Regions in the $(\kappa_\perp, \varepsilon)$-plane where surface waves exist

The regions in the $(\kappa_\perp, \varepsilon)$-plane where the surface waves exist can be defined using the graphic construction shown in Fig. 4. The Dirac point $(-\mathcal{A}_1, u_1)$ in the graphene domain 1 generates a division of the plane into four sectors. Two of them (yellow sectors in Fig. 4a) correspond to propagating waves with real $\kappa_\parallel$, and the other two sectors correspond to non-propagating waves with imaginary $\kappa_\parallel$ (white regions in Fig. 4a). A similar division of the plane is generated by the Dirac point $(-\mathcal{A}_2, u_2)$ in the domain 2. The blue sectors in Fig. 4a correspond to propagating waves in this domain.

Green regions in Fig. 4a show the overlap of the propagating-wave sectors, i.e., waves whose parameters $\kappa_\perp$ and ε lie in these overlapping green regions can simultaneously propagate in both domains. For these waves the interface between the graphene domains acts as a semitransparent barrier.

Yellow (blue) sector corresponds to the waves that can propagate only in domain 1 (only in domain 2), and the interface between the domains acts as a non-transparent (reflecting) barrier. Parameters $\kappa_\perp$ and ε of the non-propagating surface waves (i.e., waves that are evanescentin the both domains) belong to the white regions in Fig. 4a. The red solid line that connects the two Dirac points is the dispersion curve $\varepsilon(\kappa_\perp)$ described by Eq. (22). It follows from Eq. (22) that the surface waves, if exist, propagate in only one direction. In other words, *such barrier constitutes a unidirectional quantum wire.*

When the inequality (21) is not satisfied, the division of the $(\kappa_\perp, \varepsilon)$-plane has different structure, shown in Fig. 4b. Here there is no white region between the Dirac points, i. e., the surface waves are absentg in this case. Another important difference between these two cases is the following. When the inequality (21) holds, there is

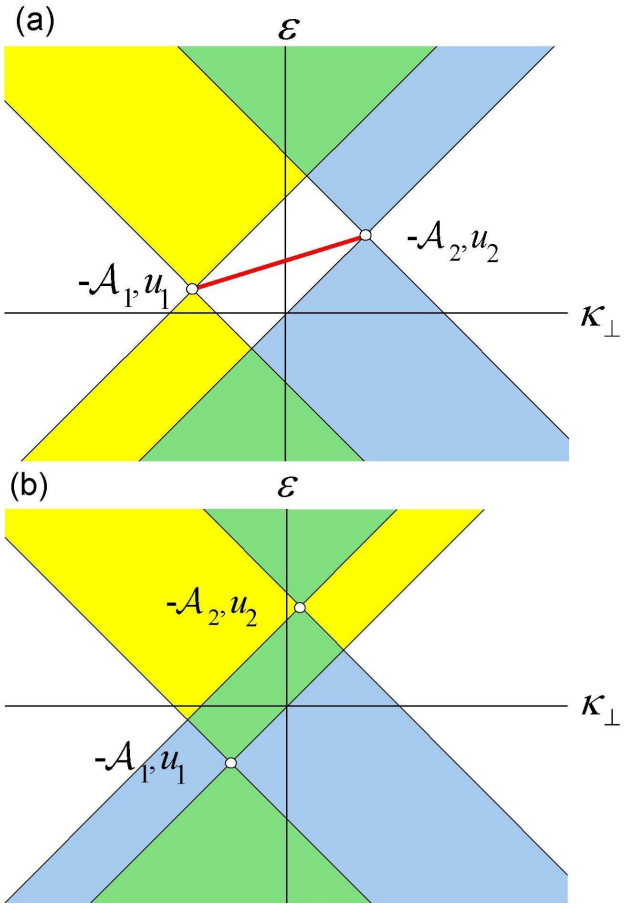

FIG. 4: (color online) The yellow and blue sectors correspond to propagating waves in domains 1 and 2, respectively. The overlapping (green) regions correspond to waves that can propagate both in domain 1 and domain 2. (a) the inequality Eq. (21) is satisfied. The barrier is opaque for all the waves whose energy lies in the energy gap between the green regions. The dispersion $\varepsilon(\kappa_\perp)$ of the surface wave is shown by the straight red line joining both Dirac points. (b) the inequality Eq. (21) is not satisfied and there is no surface wave. The barrier is semitransparent, i.e., regardless of the energy, there are always the angles of incidence when the waves penetrate through the barrier.

an energy gap, in which there are no waves penetrating through the barrier, and the barrier is opaque for all angles of incidence (all $\kappa_\perp$). Figure 4a allows easy determination of this range of energies. The absence of waves penetrating through the barrier means that the horizontal line $\varepsilon = const$ does not cross any green regions. It is readily seen that this condition is satisfied when the energy lies in the following range:

$$\frac{1}{2}(u_1 + u_2 - |\mathcal{A}_1 - \mathcal{A}_2|) < \varepsilon < \frac{1}{2}(u_1 + u_2 + |\mathcal{A}_1 - \mathcal{A}_2|).$$

When the inequality (21) is not satisfied (figure 4b corresponds to this case), any horizontal line $\varepsilon = const$ crosses some green region, i.e., there are always waves that can penetrate through the barrier.

What is important for potential applications is that the parameters of the barrier can be easily controlled by the applied voltage. Depending on the voltage, *this barrier can be either semitransparent* (Fig. 4b) *or opaque* [with bound states made of surface waves (Fig. 4a)].

IV. DOUBLE BARRIERS CAN PRODUCE WAVEGUIDES

Under certain conditions, two barriers separated by a distance d form a *waveguide*. Two barriers divide the infinite graphene sheet into tree domains: left and right infinite half-planes, and the strip (of width d) bounded by the barriers. The potentials (electric and magnetic) are constant within each domain. The values of the potentials are denoted by the sub-indices ℓ, r, and c, respectively, for left, right, and middle. Each domain is represented by its own division of the $(\kappa_\perp, \varepsilon)$-plane in sectors with propagating and non-propagating (in the given domain) waves, as it was described in the previous section. The situation is similar to those presented in Fig. 4a,b, with only one difference: now there are tree Dirac points $(-\mathcal{A}_\alpha, u_\alpha)$ $(\alpha = \ell, c, r)$ with "cones" that divide the plane on several sectors. Hereafter, the yellow-colored sectors correspond to the central (c) graphene domain, the blue-colored and violet-colored sectors correspond to the right (r) and left (ℓ) graphene domains, respectively. All overlaps of the sectors will be marked by dark blue (ℓ–r overlap), light green for the r–c overlap, green for ℓ–c overlap, and dark green for r–c–ℓ overlap.

The waveguide eigenmodes are non-propagating, evanescent waves in the left and right infinite graphene half-planes. This means that the corresponding points in the $(\kappa_\perp, \varepsilon)$-plane are located outside of the colored sectors which are generated by the r and ℓ Dirac points, i.e., in either yellow or white regions of the $(\kappa_\perp, \varepsilon)$-plane.

To simplify the presentation, we will mainly consider symmetric cases, $|u_\ell| = |u_r|$, and $|\mathcal{A}_\ell| = |\mathcal{A}_r|$ and assume, without loss of generality, that $u_c = \mathcal{A}_c = 0$.

A. Equal scalar and vector potentials: $u_\ell = u_r$ and $\mathcal{A}_\ell = \mathcal{A}_r$

We first consider the case when $u_\ell = u_r$ and $A_\ell = A_r$. Setting $u_\ell = u_r = u_2$ and $\mathcal{A}_\ell = \mathcal{A}_r = \mathcal{A}_2$ (the blue-colored sectors correspond to the r and ℓ equivalent graphene domains), and setting $u_c = u_1 = 0$ and $\mathcal{A}_c = \mathcal{A}_1 = 0$ for the central domain, one can now use Fig. 4a,b for describing the double-barrier structure.

When the inequality (21) is not valid (as in Fig. 4b), there are waveguide modes which are similar to the modes in the usual dielectric waveguides. The spectra of these modes are shown by the red lines in Fig. 5a,b for different values of the distance d between the barriers (waveguide walls).

As in a dielectric waveguide, the total internal reflection (TIR) phenomenon is responsible on the wave confinement in the central graphene domain. However, in contrast to usual dielectric waveguides, in a certain energy range there are two separate regions of $\kappa_\perp$ where TIR occurs. Decreasing the distance d between the barriers shifts the spectrum to higher-energies, with the exception of the lowest mode, which crosses the point $(-\mathcal{A}_\ell, u_\ell)$ for whatever small values of d (Fig. 5b).

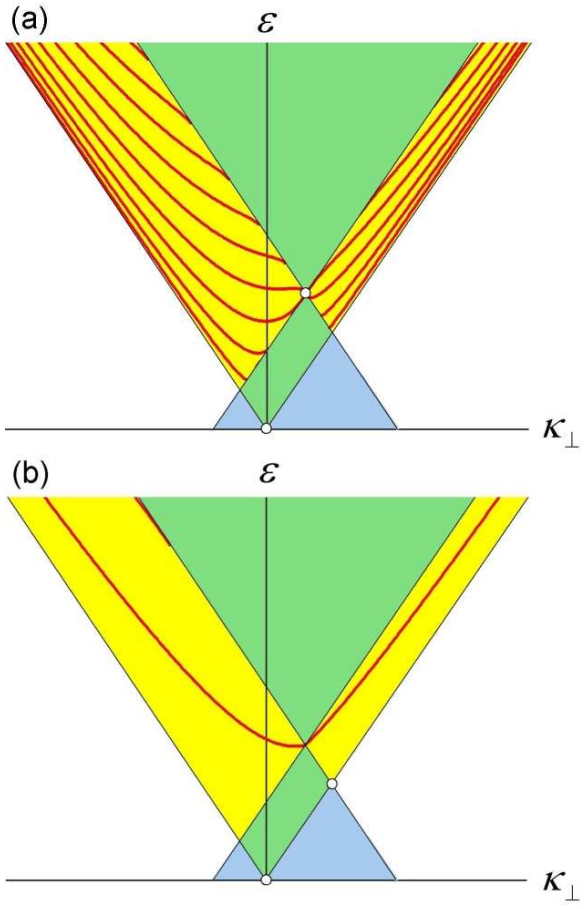

FIG. 5: (color online) Waveguide spectrum $\varepsilon(\kappa_\perp)$ (red lines) when the inequality (21) is not valid. (a) for large spacing d between the barriers; (b) for small spacing d between the barriers.

When the inequality (21) is valid, there are confined waveguide modes in the yellow regions in Fig. 4a. In addition to these "ordinary" modes, there are two "extraordinary" modes in the white region between two Dirac points where the surface wave exists. In contrast to the ordinary modes that appear due to the TIR, the extraordinary modes are formed by two coupled surface waves propagating along the barriers.

In Fig. 6a, the blue 2D "cone" on the right represents the overlap of two 2D "cones" corresponding to the left and right graphene semiplanes. The isolated red solid line originated at the right Dirac point actually represents two dispersion curves, which in this instance are

indiscernible. When these two nearly-overlapping curves approach the left Dirac point, they separate moving in opposite directions: one towards positive ε, the other towards negative ε. In other words, the two coupled surface waves propagating along the barriers (red solid curve emanating from the right Dirac point) transform smoothly into the standard ordinary modes, when approaching the left Dirac point. Examples of waveguide spectra are shown in Fig. 6a,b for different values of the distance d.

The particular case $u_\ell = u_r = 0$ has been considered in [12, 16, 32, 33], and the case $A_\ell = A_r = 0$ has been considered in [34, 35].

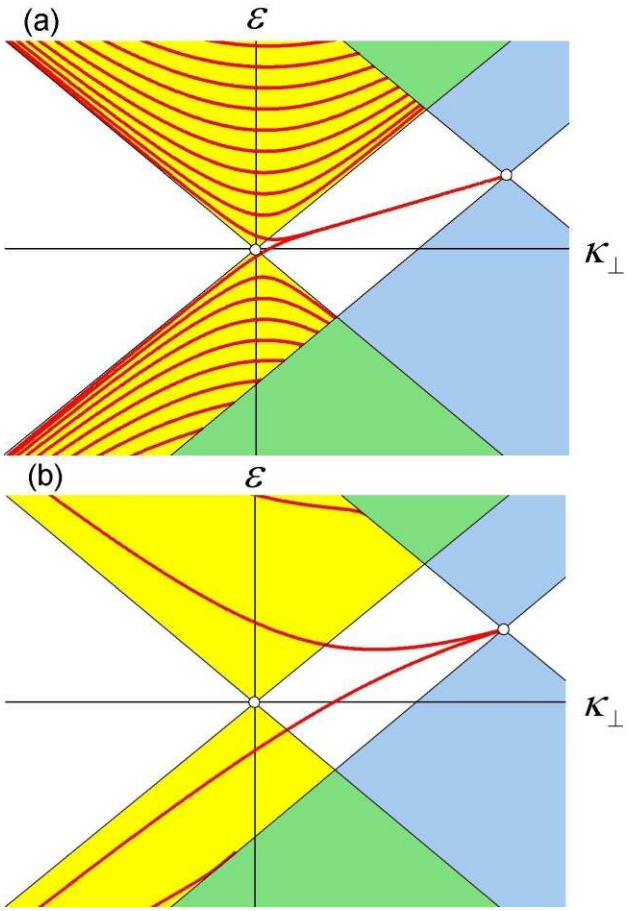

FIG. 6: (color online) Waveguide spectra (red lines) when the inequality (21) is valid. (a) large spacing d between the barriers. The isolated red line in (a) involves two extraordinary modes, corresponding to edge states, which merge in the isolated red line because these two curves are very close to each other. The difference between these nearly-overlapping modes is visible only when the modes are transformed into ordinary ones. (b) small spacing d between the barriers. Note that the spacing between the energy levels increases when the spacing decreases.

The eigenspectrum of both ordinary and extraordinary modes is defined by the requirement that a round trip phase

$$\phi = 2\mathrm{Re}(\kappa_\parallel)d + \phi_\ell + \phi_r,$$

(ϕ_ℓ and ϕ_r are the phase shifts at the reflection from the left and right barriers) is either equal to zero (extraordinary evanescent modes) or to a multiple of $2\pi n$, $n = 1, 2, \ldots$ (ordinary propagating modes).

There is an important difference between the ordinary and extraordinary modes: when the distance between the barriers is large enough, the extraordinary modes are *unidirectional* waves (see Fig. 6a). This means that all the waves (in the extraordinary mode existence region) propagate in one direction, making this mode *resistant to backscattering*, and therefor robust against y-dependent disorder. Indeed, any rather smooth obstacle in the waveguide cannot produce counter-propagating waves. As to the fluctuations of the height of the potentials (in x-direction), in principle, they can affect dramatically the propagation *across* the barriers, but have practically no influence on the waveguide eigenmodes. Note that the properties of the waveguide eigenmodes are easily controlled by the electrostatic potentials.

The closeness of two extraordinary waves spectra (central isolated red line in Fig. 6a) stems from the chosen symmetry of the waveguide potentials $u_\ell = u_r$. When this symmetry is broken, $u_\ell \neq u_r$, the difference between the spectra is clearly visible (two central red lines in Fig 7a). When the potentials u_ℓ and u_r have opposite signs, surface waves propagate along the barriers in opposite directions. As a result, two extraordinary modes not only have separated spectra, but propagate in opposite directions, as it is shown in Fig 7b. The backscattering is also suppressed in this case because the counter-propagating waves are localized mainly near the corresponding barriers.

B. Equal scalar potentials and antiparallel vector potentials: $u_\ell = u_r$ and $\mathcal{A}_\ell = -\mathcal{A}_r$

In this subsection, we will concentrate on the case when Eq. (21) is valid. The instance when the inverse of the (21) inequality is valid is similar to one considered in subsection IV A, just with a more complex division of the ($\kappa_\perp$, ε)-plane in regions.

The condition $u_\ell/\mathcal{A}_\ell = -u_r/\mathcal{A}_r$ means that the surface waves along the left and right barriers propagate in opposite directions making the waveguide eigenmodes spectra symmetric, as shown in Fig. 8a,b.

In contrast to the case of equal potentials (subsection IV.b) the spectra of ordinary and extraordinary modes are separated: there is no transformation of one kind of mode into another, as it is seen in Fig. 6 and Fig. 7. Note that the coupling between two surface waves, which produces the extraordinary mode does not split the mode energy, as it happens when $u_\ell = u_r$ and $\mathcal{A}_\ell = \mathcal{A}_r$.

There is an energy range where only extraordinary modes form the charge flux along the waveguide. De-

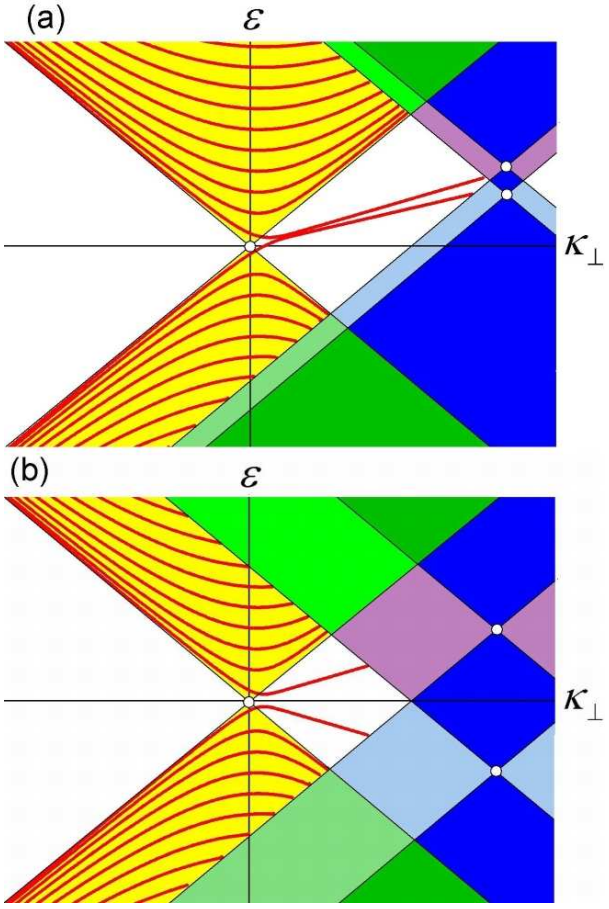

FIG. 7: (color online) Waveguide spectra for the cases discussed in the subsection IV A. (a) for $u_\ell \neq u_r$, $\mathrm{sgn}(u_\ell) = \mathrm{sgn}(u_r)$; (b) for $u_\ell = -u_r$. The difference between the two extraordinary modes is distinctly visible. For the case $\mathrm{sgn}(u_\ell) = -\mathrm{sgn}(u_r)$, the modes in (b) have opposite-directed group velocities.

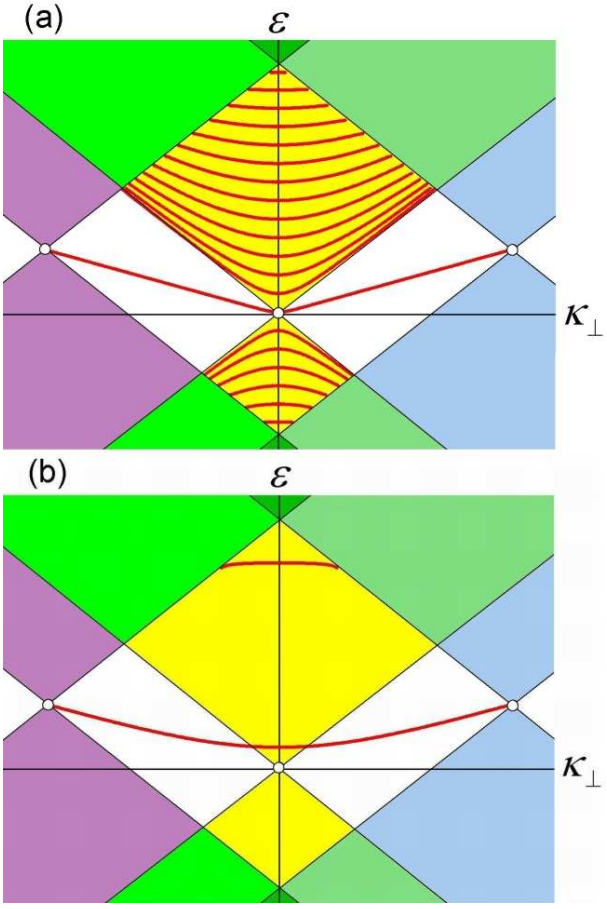

FIG. 8: (color online) Waveguide spectra when the scalar $u_\ell = u_r$ and vector $\mathcal{A}_\ell = -\mathcal{A}_r$ potentials satisfy these relations. (a) large distance d between the barriers; and (b) small distance between the barriers. When the distance d decreases, the ordinary modes are pushed out from the yellow regions and only the extraordinary mode remains in a broad energy gap.

spite the fact that the extraordinary modes are not unidirectional, the backscattering is also suppressed in this case. The reason for this is the spatial separation of regions with opposite direction of the flux: the wave functions that correspond to opposite directions of flux are localized near different (left or right) barriers. This is illustrated in Fig. 9, where the normalized flux densities for extraordinary eigenmodes with opposite wave vectors $\kappa_{\perp 1} = -\kappa_{\perp 2}$ (opposite total fluxes) are shown.

Decrease of the spacing, $d \to 0$, broadens the energy gap where only extraordinary mode exists (see Fig. 9b). The dispersion curve is then flattened and tends to the line $\varepsilon(\kappa_\perp) = u_\ell = u_r$.

C. Scalar potentials of opposite signs and antiparallel vector potentials: $u_\ell = -u_r$ and $\mathcal{A}_\ell = -\mathcal{A}_r$

When $u_\ell = -u_r$, $\mathcal{A}_\ell = -\mathcal{A}_r$ and the inequality (21) holds, both barriers support surface waves with the same direction of the charge flux. Accordingly, the flux which is associated with the extraordinary waves is unidirectional, i.e., is independent on sign of $\kappa_\perp$. Examples of waveguide spectra are shown in Fig. 10a,b. When the distance d is small enough, only extraordinary waves are confined by the waveguide.

Comparing Figs. 10a and 10b, one can see that, unlike the ordinary modes, the spectrum of the extraordinary modes is *independent of the distance d between barriers*. There is a cut-off energy ε_0 for ordinary modes, i.e., the minimal modulus $|\varepsilon|$ of the energy, for which the condition $\phi = 2\pi$ is satisfied (the cut-off energy is the analog of the cut-off frequency of conventional waveguides). The cut-off energy increases when the distance d decreases, pushing out the ordinary modes from their existence region (yellow regions in Fig. 10a,b). It is interesting to note that in the graphene waveguide with variable width $d(y)$, the extraordinary mode can penetrate through an arbitrary narrow part of the waveguide, whereas all ordinary modes are reflected from it.

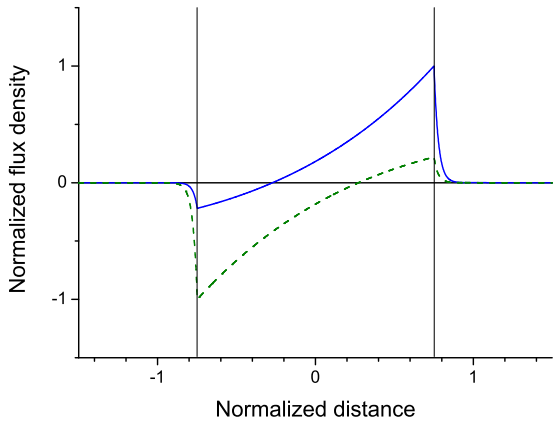

FIG. 9: (color online) Normalized current density of the extraordinary modes (counter-propagating surface waves). Solid line: $\kappa_\perp > 0$; dashed line: $\kappa_\perp < 0$. The vertical lines indicate the positions of the barriers. The counter-propagating currents are indeed spatially separated.

A similar effect (penetration of the electromagnetic wave through the waveguide waist) is typical to waveguides filled with a metamaterial with a near-zero dielectric permittivity [36]. A rather narrow waveguide is a single-mode waveguide, although its transport properties differ strongly from the usual single-mode waveguides. The transmission through this waveguide (in the frame of the model we use) is always perfect, irrespectively of smooth irregularities present on the waveguide. As in the single barrier case, the reason is the absence of counter-propagating waves that makes reflection impossible.

V. CONCLUSIONS

We have shown that crossed magnetic and electric fields applied to a narrow strip (electromagnetic barrier) on a graphene sheet can form *a unidirectional conducting channel (quantum wire)* whose properties are easily *tunable* by the voltage applied across the strip. The eigenmode of this channel is characterized by a linear dispersion and represents a one-way propagating wave. This unique property *prohibits backscattering* and therefore makes the mode *resistant to the scattering by impurities*. The classical analogy of this mode is the *drift* of a charged particle in crossed electric and magnetic fields. The transverse-localized mode exists and propagates longitudinally along the barrier with the drift velocity $v_y = v_d \equiv cE_x/H_z$ if and only if this velocity v_d is smaller than the Fermi velocity v_F: i.e., $v_d < v_F$. While one barrier forms a wire, two such barriers produce a waveguide whose eigenfunctions consist of set of ordinary and extraordinary waves. The ordinary waves are characterized by the quantization of their transverse wave numbers, while the extraordinary waves are formed by

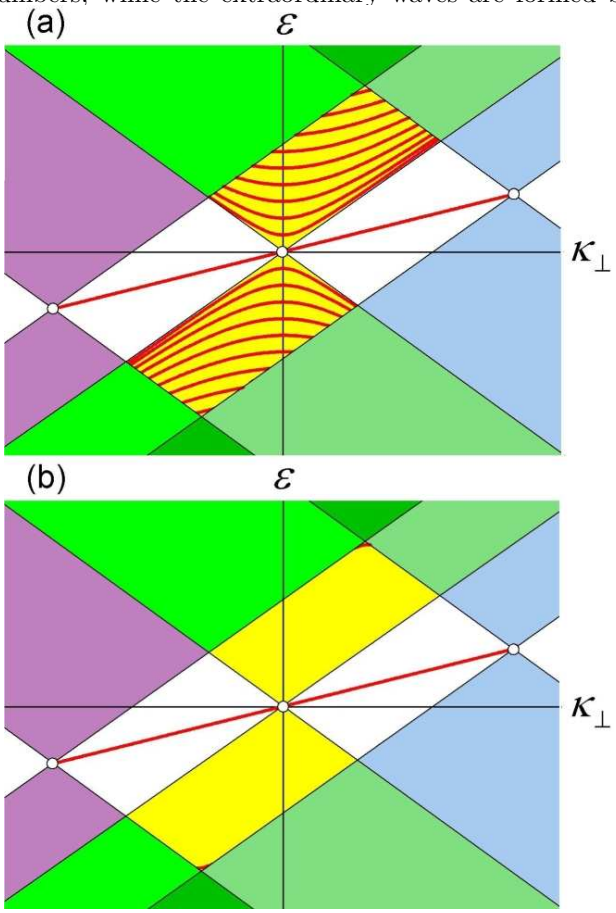

FIG. 10: (color online) Waveguide spectra for the case described in subsection IV.C, with opposite scalar and vector potentials. (a) large spacing between the barriers; (b) small spacing between the barriers.

two coupled surface waves propagating along the waveguide walls (barriers). The rather narrow waveguide has only extraordinary eigenmode. Depending on the parameters of the walls this extraordinary eigenmode can be either uni- or bi-directional. In the bi-directional case the regions with opposite directions of current flows are spatially separated, preventing backscattering and making even the bi-directional mode resistant against the scattering by impurities.

Acknowledgments

FN gratefully acknowledges partial support from the National Security Agency (NSA), Laboratory of Physical Sciences (LPS), Army Research Office (ARO), and National Science Foundation (NSF) under Grants No. 0726909 and No. JSPS-RFBR 06-02-91200.

[1] A.H. Castro Neto, F. Guinea, N.M.R. Peres, K.S. Novoselov, and A.K. Geim, Rev. Mod. Phys. **81**, 109 (2009).

[2] A.K. Geim and K.S. Novoselov, Nature Materials **6**, 183 (2007).

[3] K. Novoselov et al., Nature **438**, 197 (2005).

[4] M.I. Katsnelson, Materials Today **10**, 20 (2007).

[5] B. Trauzettel, D.V. Bulaev, D. Loss, and G. Burkard, Nature Physics **3**, 192 (2007).

[6] C. Berger, Z. Song, T. Li et al. J. Phys. Chem. B, **108**, 19912 (2004).

[7] Y.-W. Son, M.L. Cohen, and S.G. Louie, Nature **444**, 347 (2006).

[8] O. Klein, Z. Phys. **53**, 157 (1929).

[9] M.I. Katsnelson, K.S. Novoselov, and A.K. Geim, Nature Physics **2**, 620 (2006).

[10] A. De Martino, L. Dell´Anna, and R. Egger, Phys. Rev. Lett. **98**, 066802 (2007).

[11] A. De Martino, L. Dell´Anna, and R. Egger, Solid Stat. Commun. **144**, 547 (2007).

[12] V.M. Pereira and A.H. Castro Neto, Phys. Rev. Lett. **103**, 046801 (2009).

[13] F. Guinea, M.I. Katsnelson, and A.K. Geim, Nature Physics **6**, 30 (2010); arXiv:cond-mat/0909.1787

[14] M.M. Fogler, F. Guinea, and M.I. Katsnelson, Phys. Rev. Lett. **101**, 226804 (2008).

[15] M. Ramezani Masir, P. Vasilopoulos, A. Matulis, and F. M. Peeters, Phys. Rev. B **77**, 235443 (2008).

[16] M. Ramezani Masir, A. Matulis, and F.M. Peeters, Phys. Rev. B **79**, 155451 (2009).

[17] A. Kormányos, P. Rakyta, L. Oroszlány, and J. Cserti, Phys. Rev. B **78**, 045430 (2008).

[18] S. Park and H.-S. Sim, Phys. Rev. B **77**, 075433 (2008).

[19] J.E. Müller, Phys. Rev. Lett. **68**, 385 (1992).

[20] L. Oroszlány, P. Rakyta, A. Kormányos, C.J. Lambert, and J. Cserti, Phys. Rev. B **77**, 081403(R) (2008).

[21] T.K. Ghosh, A. De Martino, W. Häusler, L. Dell´Anna, and R. Egger, Phys. Rev. B **77**, 081404(R) (2008).

[22] F.M. Peeters and A. Matulis, Phys. Rev. B **48**, 15166 (1993).

[23] J. Reijniers and F.M. Peeters, Phys. Rev. B. **63**, 165317 (2001).

[24] J. M. Pereira Jr., F.M. Peeters, and P. Vasilopoulos, Phys. Rev. B **75**, 125433 (2007).

[25] M. Titov, Eur. Phys. Lett. **79**, 17004 (2007).

[26] Y.P. Bliokh, V. Freilikher, S. Savel'ev, and F. Nori, Phys. Rev. B **79**, 075123 (2009).

[27] A.V. Rozhkov, S.S. Savel'ev, and F. Nori, Phys. Rev. B **79**, 125420, (2009).

[28] F. Zhai and K. Chang, Phys. Rev. B **77**, 113409 (2008).

[29] R. Kubrak, A. Neumann, B.L. Gallagher, P.C. Main, M. Henini, C.H. Marrows, and B.J. Hickey, J. Appl. Phys. **87**, 5986 (2000).

[30] M. Cerchez, S. Hugger, T. Heinzel, and N. Schulz, Phys. Rev. B **75**, 035341 (2007).

[31] S.D. Bader, Rev. Mod. Phys. **78**, 1 (2006).

[32] M. Ramezani Masir, P. Vasilopoulos, and F. M. Peeters, New J. Phys. **11**, 095009 (2009).

[33] S. Ghosh and M. Sharma, J. Phys.: Condens. Matter **21**, 292204 (2009); S. Ghosh and M. Sharma, arXiv:cond-mat/0806.2951 (2009).

[34] V.A. Yampol'skii, S. Savel'ev, and F. Nori, New J. Phys. **10**, 053024 (2007).

[35] V.A. Yampol'skii, S.S. Apostolov, Z.A. Maizelis, A. Levchenko, and F. Nori, arXiv:cond-mat/0903.0078 (2009).

[36] M. Silveirinha and N. Engheta, Phys. Rev. Lett. **97**, 157403 (2006).